Subnano-transformation of Molybdenum Carbide to Oxycarbide

Journal:	*Nanoscale*
Manuscript ID	NR-ART-06-2020-004495.R1
Article Type:	Paper
Date Submitted by the Author:	13-Jul-2020
Complete List of Authors:	Wakizaka, Masanori; TIT Atqa, Augie; TIT Chun, Wang-Jae; ICU Imaoka, Takane; TIT Yamamoto, Kimihisa; TIT

ARTICLE

Subnano-transformation of Molybdenum Carbide to Oxycarbide

Masanori Wakizaka,[a] Augie Atqa,[a] Wang-Jae Chun,[b] Takane Imaoka *[a] and Kimihisa Yamamoto *[a]

Received 00th January 20xx,
Accepted 00th January 20xx

DOI: 10.1039/x0xx00000x

Ultrasmall particles exhibit structures and/or properties that are different from those of the corresponding bulk materials; in this context especially ultrasmall precious-metal particles have been extensively investigated. In this study, we targeted the transition base-metal Mo and succeeded in systematically producing Mo oxycarbide/carbide particles with diameters of 1.7 ± 0.7, 1.4 ± 0.5, 1.3 ± 0.4, 1.2 ± 0.3, 1.0 ± 0.3, and 0.8 ± 0.2 nm on a carbon support using the carbothermal hydrogen reduction method at 773 K and a diphenylazomethine-type dendrimer as a template. The formation and properties of the particles were confirmed using x-ray photoelectron spectroscopy, high-angle annular dark-field scanning transmission electron microscopy (HAADF-STEM) images, and x-ray absorption fine structure (XAFS) studies. We found that Mo particles with a diameter of 1.3 nm or greater formed carbides such as β'-Mo_2C, whereas smaller particles formed oxycarbides, indicating a size-dependent transformation in the phase or composition of the particles. Thus, this work demonstrated a new concept, subnano-transformation, which would be a new class of phase transformation based on the concept of the size dependence in such an ultrasmall scale. In addition, the movement of Mo atoms within a cluster and on the fringes of a nanoparticle was also demonstrated during continuous time-course high-resolution HAADF-STEM observation.

Introduction

Ultrasmall particles are fascinating materials that exhibit structures and/or properties that are different to those of the corresponding bulk material.[1-16] For example, Buffat *et al.*[1] reported that the melting point of Au nanoparticles is drastically decreased compared to that of bulk Au, while Kitagawa *et al*. reported that Ag and Rh metal atoms could be mixed at the atomic level in nanoparticles,[17,18] whereas those in the bulk formed completely separated phases. These sophisticated studies strongly suggest that the interactions between metal atoms, the phase stability, and the properties of these materials depend on the particle size. Additionally, Au atoms have been reported to move within clusters or on the fringes of a nanoparticle during observation using transmission electron microscopy (TEM),[19-21] clearly indicating flexible structures of these ultrasmall particles. Although many precious-metal clusters and nanoparticle systems have been fabricated, those containing transition base-metals with metal-to-metal interactions or bonds have remained elusive.

Molybdenum carbide is a very robust and stable substance with a high melting point of ~2960 K.[22] Although it is sometimes classified as a ceramic composed of Mo and C, it is also classified as an alloy system with metal-to-metal bonds between Mo.[22-26] Matteazzi *et al*. obtained Mo carbide nanoparticles with a size of ~20 nm by mixing elemental Mo and C using a mechanical alloying technique at room temperature.[27] Moreover, several chemical reduction methods have been reported, including carbothermal hydrogen reduction (CHR). Mo combines readily with C atoms derived from carbon sources such as carbon supports,[28-33] organic polymers,[34] or organic ligands[35] during calcination. As hydrogen promotes the reduction and carbonization of Mo precursors such as Mo oxides or complexes, the use of the CHR method decreases the Mo carbide formation temperature compared to that in conventional carbothermal reductions. The production of ultrasmall Mo carbide particles has been attempted in many studies;[27-40] however, to date, Mo particles with a diameter of ~1 nm or less have not been successfully produced, except for those detected in the gas phase.[41,42]

Dendritic phenylazomethine (DPA)-type dendrimers (Figure S1) are one of the types of macromolecules most commonly used as precursors for clusters.[43-47] DPA dendrimers assemble metal ions or metal salts by coordinating them at their imine sites in a stepwise and radial fashion, from the center outward. For example, tetraphenylmethane-core DPA dendrimer generation 4 (TPM-DPAG4) has 4, 8, 16, and 32 imines in each site, which can coordinate 4, 12, 28, or 60 metal atoms. These metal precursors produce precisely size-controlled clusters of ~1 nm or less with a relatively narrow size distribution through chemical reduction and fixation on a support. We have previously established a method for the assembly of $MoCl_5$ into TPM-DPAG4,[47] and these assemblies could be used as precursors for the synthesis of Mo carbide clusters. In the present study, we aimed to produce Mo carbide nanoparticles and clusters with diameters of 1–2 nm or less in order to reveal whether such ultrasmall Mo carbide clusters are stable. In addition, the movement of Mo atoms within a cluster and

---

[a] Laboratory for Chemistry and Life Science Institute of Innovative Research, Tokyo Institute of Technology, Yokohama 226-8503, Japan.
[b] Graduate School of Arts and Sciences, International Christian University, Tokyo 181-8585, Japan.

Electronic Supplementary Information (ESI) available: Additional methods, PXRD, XPS, XAFS, RWGS data, a HAADF-STEM image and a histogram, contour graphs, and Equations are listed. See DOI: 10.1039/x0xx00000x nanoparticle was demonstrated for the first time under electron beam irradiation.

Experimental

Materials

TPM-DPAG4 was prepared according to previously reported procedures.[47] $MoCl_5$, 3-chloropyridine (3-Clpy), β'-Mo_2C, boron nitride (BN), and graphitized mesoporous carbon (GMC) were purchased from Sigma-Aldrich. β'-Mo_2C was used as-purchased for x-ray absorption fine structure (XAFS) and catalysis, whereas β'-Mo_2C/C was synthesized for x-ray photoelectron spectroscopy (XPS, see Methods in the ESI). Graphene nanopowder (GNP) with a thickness of ~1.6 nm was purchased from Alliance Biosystems Inc. MoO_3 and MoO_2 were purchased from Fujifilm Wako Pure Chemical Corp. Dehydrated dichloromethane (CH_2Cl_2), dehydrated tetrahydrofuran (THF), dehydrated *n*-hexane, dehydrated pyridine (py), dehydrated acetonitrile (CH_3CN), methanol (MeOH) and molecular sieves 3A (MS3A) were purchased from Kanto Chemical Co., Inc. Prior to use, MS3A was washed with tap water and distilled water before being dried at 373 K for more than 24 h *in vacuo*. All dehydrated solvents were treated with MS3A for further dehydration prior to use. The GMC was washed with distilled water and MeOH, followed by filtration and drying *in vacuo*. Subsequently, the GMC was heated for 3 h to 1173 K under a flow (200 mL min^{-1}) of H_2 (99.99999%).

Preparation of the samples

Mo nanoparticles. THF (5.0 mL) was added into the vessel containing $MoCl_5$ (0.26, 0.13, or 0.075 mmol) and GMC (100 mg) under an atmosphere of dry Ar. The suspension was dispersed under sonication (30 W) for 3 min, then stirred for 30 min. Following evaporation, the powder samples of **Mo-NP(a)/C**, **Mo-NP(b)/C**, and **Mo-NP(c)/C** were dispersed in *n*-hexane (5 mL), filtered, washed with *n*-hexane (2 × 5 mL) and dried *in vacuo* for 2 h, respectively.

Mo clusters. A pale yellow CH_2Cl_2/THF = 2/1 (*v*/*v*) solution (180 mL) of TPM-DPAG4 (30.0, 12.9, or 9.00 μM) in the presence of py (4 eq.) and 3-Clpy (40 eq.) was prepared under an atmosphere of dry Ar at 245 K. Subsequently, the THF solution of $MoCl_5$ (12, 28, or 60 eq.) was added to the solution. After stirring for 45 min at 245 K, the solution turned deep yellow. The solution was dropped with stirring into the GMC (540 mg) suspension in CH_2Cl_2 (20 mL), which was dispersed under sonication (30 W) for 3 min. After filtration, the powder samples (**Mo_{12}/C**, **Mo_{28}/C**, and **Mo_{60}/C**) were washed with *n*-hexane (2 × 5 mL) and dried *in vacuo* for 2 h, respectively.

Mo_{60}-aggregated particles. A pale yellow CH_2Cl_2/THF = 2/1 (*v*/*v*) solution (163 mL) of TPM-DPAG4 (9.00 μM) was prepared as the same procedure above, and the THF solution of $MoCl_5$ (60 eq.) was added to the solution. After stirring for 45 min at 245 K, the solution was dropped with stirring into the GMC (76 mg) suspension in CH_2Cl_2 (10 mL), which was dispersed under sonication (30 W) for 3 min. Following evaporation, the powder sample of **Mo_{60}-aggregated/C** was dispersed in *n*-hexane (10 mL), filtered, washed with *n*-hexane (2 × 5 mL) and dried *in vacuo* for 2 h.

The sample for HAADF-STEM continuous observation. A pale yellow CH_2Cl_2/THF = 2/1 (*v*/*v*) solution (4.5 mL) of TPM-DPAG4 (3.00 μM) was prepared as the same procedure above, and the THF solution of $MoCl_5$ (28 eq.) was added to the solution. After stirring for 45 min at 245 K, the solution was dropped with stirring into the GNP (13 mg) suspension in CH_2Cl_2 (1.5 mL), which was dispersed under sonication (100 W) for 3 min. After filtration, the powder sample was washed with *n*-hexane (2 × 1 mL) and dried *in vacuo* for 2 h.

Carbothermal hydrogen reduction (CHR)

Samples were calcined at 773 or 1173 K for 30 min under an H_2 (99.99999%, 100 mL min^{-1}) atmosphere on a quartz boat in a furnace at a heating rate of 24 K min^{-1}. Both before and after the calcination, the samples were handled under an Ar atmosphere.

Measurements

High-angle annular dark-field scanning TEM (HAADF-STEM) images and continuous time-course high-resolution HAADF-STEM images were recorded using a JEOL JEM-ARM200F ACCELARM (accelerating voltage: 80 or 200 kV) with spherical aberration corrected probe (CEOS, ASCOR) at a convergence angle of 31.8 mrad. The inner and outer collection angles used in recording the HAADF images were 68 and 280 mrad, respectively. To maintain the electron dose constantly during the time-course observations, the probe current was fixed at 26 pA while the beam scanned across a field of view (4 × 4 nm^2). The pixel size and the pixel time are 3600 pixel/nm^2 and 16 μs/pixel, respectively. After being subjected to CHR at 773 K for 30 min, the analytes were dispersed in *n*-hexane (for HAADF-STEM images) or CH_3CN (for HAADF-STEM continuous observation), dropped onto micro Cu grids with carbon filaments (Alliance Biosystems thin holey carbon film coated grids), and dried for >12 h *in vacuo* at room temperature. Powder x-ray diffraction (PXRD) measurements were carried out with Cu-Kα radiation using a Rigaku Ultima IV diffractometer at room temperature; the analyte was wrapped in a gas barrier film (silica deposited nylon/polyethylene) in an Ar atmosphere. XPS measurements were recorded on an ESCA 1700R ULVAC-PHI, and the binding energy was calibrated using C1s (284.5 eV) as the reference. XAFS spectra were measured in transmission mode at room temperature at AR-NW10A (KEK-PF, Tsukuba, Japan; ring energy: 6.5 GeV), BL01B1 (SPring-8, Hyogo, Japan; ring energy: 8.0 GeV), or BL07 (SAGA-LS, Saga, Japan; ring energy: 1.4 GeV) beamlines. X-rays were monochromated by channel-cut monochromators using a Si(311) at AR-NW10A and BL01B1 or a Si(220) at BL07, and then detected by two ionization chambers filled with Ar/N_2 (1:1) for I_0 and Ar/Kr (3:1) for I. The analytes, **Mo-NP(a)/C**, **Mo-NP(b)/C**, **Mo-NP(c)/C**, **Mo_{60}/C**, **Mo_{28}/C**, **Mo_{12}/C**, and **Mo_{60}-aggregated/C**, were packed into a glass or a vinyl chloride tube (ϕ 7 mm) and wrapped in a double gas barrier film in Ar atmosphere, whereas MoO_3, MoO_2, and β'-Mo_2C were pelletized by mixing with BN (ϕ 10 mm). The

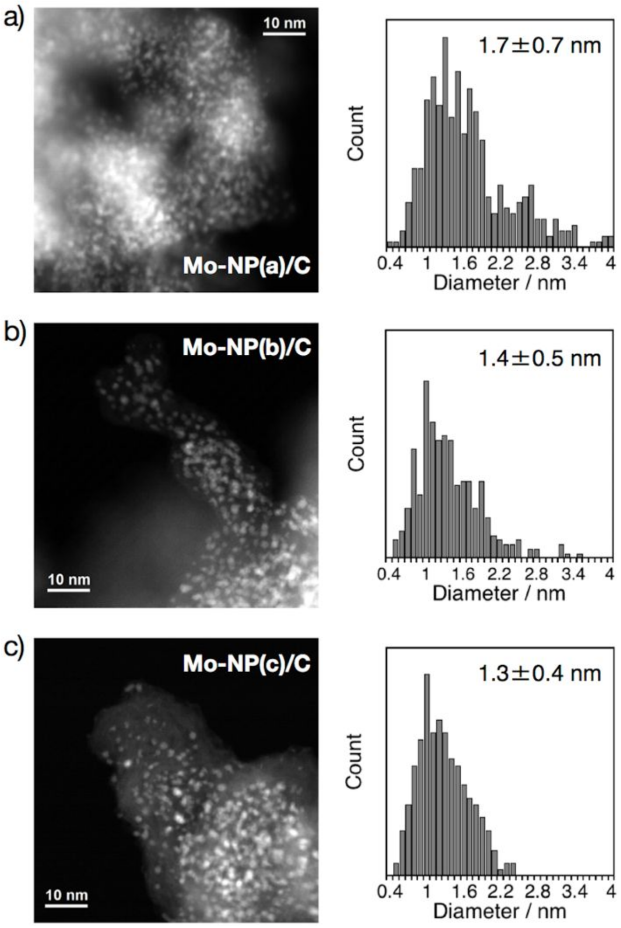

Figure 1. HAADF-STEM images and histograms of the particle size distribution of a) **Mo-NP(a)/C**, b) **Mo-NP(b)/C**, and c) **Mo-NP(c)/C** after CHR at 773 K for 30 min.

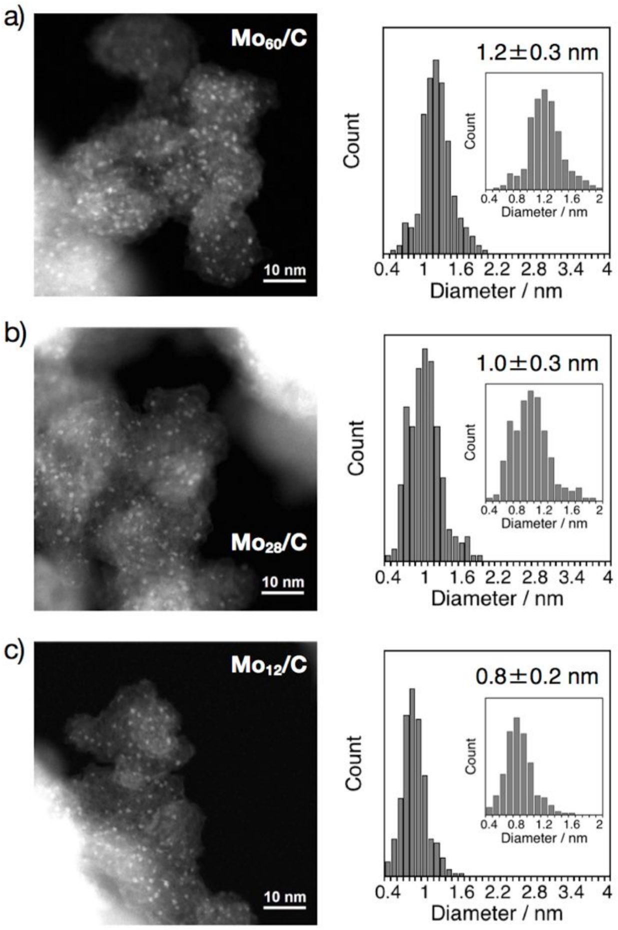

Figure 2. HAADF-STEM images and histograms of the size distribution of a) **Mo$_{60}$/C**, b) **Mo$_{28}$/C**, and c) **Mo$_{12}$/C** after CHR at 773 K for 30 min.

absorption energies of all samples were corrected by that of a Mo foil (thickness: 10 μm) as a reference for each beamline. XAFS analytical procedure is described in detail in the ESI.

Results and discussion

Size-controlled Mo nanoparticles

The PXRD pattern of **Mo-NP(a')/C** calcined at 1173 K under H$_2$ shows diffraction peaks at 2θ values of 34.25, 37.85, and 39.32° (Figure S2). These diffraction peaks were assigned to the (021)(002), (200), and (121)(102) planes of an orthorhombic structure, which corresponds to the crystal structure of β'-Mo$_2$C.[22] The observation of β'-Mo$_2$C demonstrated that the MoCl$_5$ on the GMC could be reduced by hydrogen and carbonized with the GMC support and/or adsorbed THF as the carbon source during CHR at 1173 K. The crystal size of the Mo carbide was estimated to be ~31 nm using Scherrer's equation (Equation S1), which indicated that aggregation and sintering of the product occurred during CHR.

To inhibit this aggregation and sintering, CHR experiments were carried out at lower temperature. XPS data demonstrated that the precursors could be reduced at 773 K (Figure S3). Figure 1 shows the HAADF-STEM images and histograms of the particle size distribution of **Mo-NP(a)/C**, **Mo-NP(b)/C**, and **Mo-NP(c)/C** after CHR at 773 K. In each sample, Mo nanoparticles were found to be dispersed on the carbon support. The mean diameters and standard deviations of the particles of **Mo-NP(a)/C**, **Mo-NP(b)/C**, and **Mo-NP(c)/C** were estimated to be 1.7 ± 0.7, 1.4 ± 0.5, and 1.3 ± 0.4 nm, respectively. Therefore, the size of Mo nanoparticles could be controlled by varying the loading of Mo, *i.e.*, by using 2.6, 1.3, and 0.75 mmol$_{\mathrm{Mo}}$ g$_{\mathrm{GMC}}^{-1}$ before CHR.

Precisely size-controlled Mo clusters

To produce precisely size-controlled particles smaller than those formed in **Mo-NP(c)/C**, TPM-DPAG4 loaded with 60, 28, and 12 eq. of MoCl$_5$ was used as a precursor.[47] HAADF-STEM images and histograms of the particle size distribution of **Mo$_{60}$/C**, **Mo$_{28}$/C**, and **Mo$_{12}$/C** after CHR at 773 K are shown in Figure 2. Mo clusters with sizes of ~1 nm were obtained on the carbon support. The mean particle diameter and standard deviation were estimated to be 1.2 ± 0.3, 1.0 ± 0.3, and 0.8 ± 0.2 nm for **Mo$_{60}$/C**, **Mo$_{28}$/C**, and **Mo$_{12}$/C**, respectively. The particle-size distributions of these samples were comparatively controlled by fixation on the carbon support before reduction despite the lability of the macromolecule complexes in solution. Previously, the smallest reported Mo particles were those of Janiak *et al.*[48] and Feldmann *et al.*[49] with sizes of 1.5 ± 0.3 and

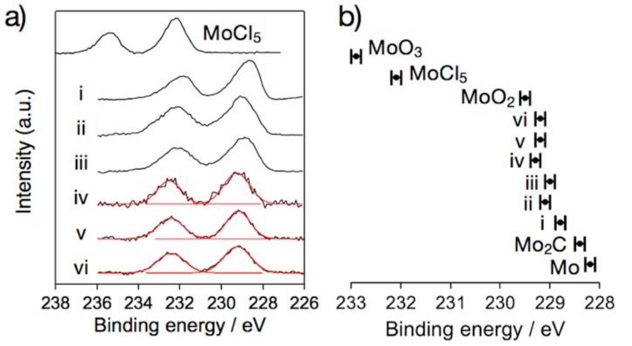

Figure 3. a) XPS spectra (black lines) in the range of the binding energies for Mo $3d_{3/2}$ and $3d_{1/2}$ with fitting curves (red lines). b) Plots of the Mo $3d_{3/2}$ binding energy of i) **Mo-NP(a)/C**, ii) **Mo-NP(b)/C**, iii) **Mo-NP(c)/C**, iv) **Mo_{60}/C**, v) **Mo_{28}/C**, and vi) **Mo_{12}/C** after CHR at 773 K for 30 min, along with those of $MoCl_5$, β'-Mo_2C/C as-synthesized, Mo (powder), MoO_2, and MoO_3.[47] Binding energies were calibrated by setting the C 1s peak of GMC to 284.5 eV, and the experimental error was estimated to be ± 0.1 eV.

1.5 ± 0.4 nm, respectively; therefore, the particles in this study represented the smallest size-controlled Mo particles as confirmed by TEM or STEM to date.

Figure 3 shows the XPS data for **Mo-NP(a)/C**, **Mo-NP(b)/C**, **Mo-NP(c)/C**, **Mo_{60}/C**, **Mo_{28}/C**, and **Mo_{12}/C** after CHR at 773 K. The starting material $MoCl_5$ shows peaks at binding energies of 232.2 and 235.4 eV, which were assigned as the $3d_{3/2}$ and $3d_{1/2}$ peaks of Mo(V), respectively. In contrast, in the **Mo-NP(a)/C** spectrum, these peaks appear at lower binding energies of 228.8 and 232.0 eV, suggesting the presence of Mo carbide after CHR. Similarly, the locations of these peaks in the **Mo-NP(b)/C** (229.1 and 232.2 eV), **Mo-NP(c)/C** (229.0 and 232.1 eV), **Mo_{60}/C** (229.3 and 232.5 eV), **Mo_{28}/C** (229.2 and 232.4 eV), and **Mo_{12}/C** (229.2 and 232.4 eV) spectra clearly indicate the reduction of the $MoCl_5$ precursors during CHR. The Mo $3d_{3/2}$ binding energies of these samples were located between those of β'-Mo_2C (228.4 and 231.6 eV, Figure S3) and MoO_2 (229.5 and 232.7 eV),[47] indicating that their electronic states were different from those of both bulk of β'-Mo_2C and MoO_2. Their slightly higher binding energies compared to that of β'-Mo_2C suggest a possible particle-size effect,[50] crystallinity, and/or a change in the charge transfer based on the chemical structure.[51]

Particle-size dependence of the local structure around Mo.

None of the samples exhibited any PXRD peaks after being subjected to CHR at 773 K due to their small particle size, low crystallinity, and/or low Mo content. Therefore, we used XAFS to investigate the local structure around Mo for each particle size. Figures 4a, 4b, and S4 show the x-ray absorption near edge structure (XANES) spectra of Mo–K edge and their first derivatives for **Mo-NP(a)/C**, **Mo-NP(b)/C**, **Mo-NP(c)/C**, **Mo_{60}/C**, **Mo_{28}/C**, and **Mo_{12}/C** after CHR at 773 K. The spectra of **Mo-NP(a)/C** and **Mo-NP(b)/C** are very similar to that of β'-Mo_2C, suggesting the carbonization of Mo during CHR. On the other hand, those of **Mo_{60}/C**, **Mo_{28}/C**, and **Mo_{12}/C** are slightly different to those of β'-Mo_2C; however, the features of the white line are very similar to those of the carbide, and quite different to those of the oxides MoO_2 and MoO_3.

The corresponding extended x-ray absorption fine structure (EXAFS) spectra are shown in Figures 4c and 4d. β'-Mo_2C exhibits two peaks in the *r* regions of 1–2 and 2–3 Å, which were assigned to the waves of Mo–C and Mo–Mo, respectively. Curve fitting of the EXAFS data was carried out for the Mo–Mo bond, because the Mo–Mo bond distance is more sensitive to the chemical structure around Mo than that of the Mo–C bond. Although eight kinds of Mo–Mo bond distances of 2.904–3.035 Å have been observed crystallographically for β'-Mo_2C,[22] the curve fitting of the EXAFS data was applied with the Mo–Mo bond as one component given that the corresponding individual EXAFS waves are indistinguishable at the present resolution. Thus, a Mo–Mo bond distance of 2.98 ± 0.01 Å was obtained from the curve fitting (Table 1); this value is comparable to that of the mean value obtained from crystallography. The coordination number (*N*) for Mo–Mo (*N* = 9.6 ± 0.7) obtained from the EXAFS data is slightly lower than the crystallographically determined value (*N* = 12), suggesting a cancellation of the EXAFS amplitude[52] due to interference between the waves derived from the different length of Mo–Mo bonds (Table S1). The EXAFS spectrum of **Mo-NP(a)/C** in this region strongly resembles that of β'-Mo_2C. The Mo–Mo bond

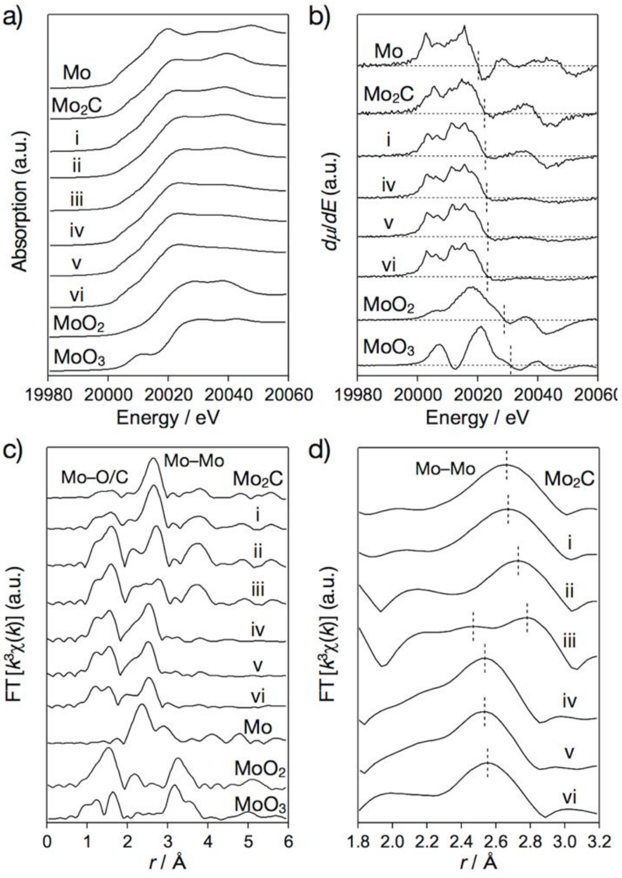

Figure 4. a) Mo–K edge XANES spectra, b) first derivative of the XANES spectra, c) full-range EXAFS spectra, and d) magnification of the EXAFS spectra in the region *r* = 1.8-3.2 Å for i) **Mo-NP(a)/C**, ii) **Mo-NP(b)/C**, iii) **Mo-NP(c)/C**, iv) **Mo_{60}/C**, v) **Mo_{28}/C**, and vi) **Mo_{12}/C** after CHR at 773 K for 30 min, together with those of Mo (foil), β'-Mo_2C, MoO_2, and MoO_3. The first derivative spectra measured using a Si(311) monochromator are shown in b), whereas those obtained using a Si(220) monochromator are shown in Figure S4.

Table 1. Summary of the EXAFS curve fitting data

Sample	Pair	N	Distance / Å	σ^2 / 10^{-3} Å^2	ΔE_0 / eV	R_f / %
β'-Mo_2C	Mo–Mo	9.6 ± 0.7	2.98 ± 0.01	6.2 ± 0.3	–1.4 ± 0.7	0.1
Mo-NP(a)/C	Mo–Mo	6.5 ± 1.4	2.98 ± 0.01	9.0 ± 1.2	0.7 ± 1.9	1.1
Mo-NP(b)/C	Mo–Mo	6.8 ± 4.6	2.97 ± 0.03	15.8 ± 5.1	1.0 ± 4.6	7.9
Mo_{60}/C	Mo–Mo	1.3 ± 0.6	2.85 ± 0.02	6.6 ± 2.4	–3.3 ± 5.2	3.8
Mo_{28}/C	Mo–Mo	1.3 ± 0.8	2.85 ± 0.02	7.2 ± 2.4	–3.3 ± 5.9	5.2
Mo_{12}/C	Mo–Mo	1.3 ± 0.5	2.86 ± 0.02	8.1 ± 2.0	–0.5 ± 3.8	2.6

An inelastic reduction factor of S_0^2 = 1.0 for Mo–Mo was estimated from the amplitude of the Mo foil, in which the coordination numbers of bcc Mo are 8 and 6. All curve fitting was applied in k space (k = 3–14 Å^{-1}), and a Fourier filtering was applied in r = 2.1–3.0 (β'-Mo_2C and **Mo-NP(a)/C**), 2.2–3.0 (**Mo-NP(b)/C**), and 2.1–2.9 (**Mo_{60}/C**, **Mo_{28}/C**, **Mo_{12}/C**), respectively.

distance for **Mo-NP(a)/C** (2.98 ± 0.01 Å) was estimated based on the curve fitting, indicating that the structure around Mo is identical to that in β'-Mo_2C. **Mo-NP(b)/C** also showed the same Mo–Mo bond distance as β'-Mo_2C and was thus assigned as Mo carbide. On the other hand, the N value of **Mo-NP(b)/C** (N = 6.8 ± 4.6) exhibited a relatively large error as well as a relatively large Debye–Waller factor ($\sigma^2 = 15.8 \pm 5.1 \times 10^{-3}$ Å^2), suggesting a structural disorder. Presumably, this structural disorder originates from the co-existence of a small amount of other Mo species. The EXAFS peak of the Mo–Mo bond in **Mo-NP(c)/C** was split into two overlapping peaks corresponding to two different Mo–Mo bonds. A curve fitting could not be applied due to the prohibitively increased number for the fitting parameter, while the co-existence of two different environments around Mo was clearly demonstrated. On the other hand, curve fitting of **Mo_{60}/C**, **Mo_{28}/C**, and **Mo_{12}/C** exhibited only one peak assigned to the Mo–Mo bond at 2.85 ± 0.02, 2.85 ± 0.02, and 2.86 ± 0.02 Å, respectively. These Mo–Mo bond distances are significantly shorter than that of β'-Mo_2C. The N values of 1.3 ± 0.6, 1.3 ± 0.8, and 1.3 ± 0.5 for **Mo_{60}/C**, **Mo_{28}/C**, and **Mo_{12}/C**, respectively, suggest di- or tri-nuclear structures, even though those proposed N values would be insufficient nuclear numbers to produce the clusters with diameters of 1.2 ± 0.3, 1.0 ± 0.3, and 0.8 ± 0.2 nm, respectively. We thus concluded that these N values cannot be determined unequivocally due to the possibility of cancellation of the EXAFS amplitude by indistinguishable overlapping components.

Although the Mo–Mo bond distances in all clusters, *i.e.*, **Mo_{60}/C**, **Mo_{28}/C**, and **Mo_{12}/C**, are shorter than those of Mo carbide, they are clearly longer than the 2.73 ± 0.01 Å bonds in metallic Mo (Table S1). The elongation of the Mo–Mo bond relative to those in metallic Mo can be reasonably explained by the presence of bridging atoms such as C or O, which have atomic radii of 0.67 and 0.48 Å, respectively.[53] For instance, Mo–Mo bonds with bridging O atoms exhibit a mean length of 2.81 Å in MoO_2,[54,55] whereas the C atoms in β'-Mo_2C elongate the mean bond length to 2.97 Å.[22,55] Ferguson *et al.*[56] and Oyama *et al.*[57] have reported that Mo oxycarbide exhibits a face-centered cubic crystal structure with a values of 4.15–4.18 and 4.1 Å and estimated Mo–Mo distances of 2.93–2.96 and 2.9 Å, respectively. In addition, Iwasawa *et al.*[58] and Faro *et al.*[59] have reported EXAFS studies on Mo oxycarbide clusters with Mo–Mo bond distances of 2.84 ± 0.03, 2.86 ± 0.04, and 2.92 ± 0.02 Å. The Mo–Mo bond distances in **Mo_{60}/C**, **Mo_{28}/C**, and **Mo_{12}/C** fall within these ranges, suggesting a Mo oxycarbide structure. In order to support this assignment for an oxycarbide, reverse water gas shift (RWGS) reactions were carried out (Figure S5 and Table S2). It was revealed that Mo carbides (β'-Mo_2C and **Mo-NP(b)/C**) and MoO_2 delivered activation energies of ~60 and ~150 kJ mol^{-1}, respectively. The results of these reactions suggest that Mo oxide exhibits a low catalytic activity, albeit that carbonization of the catalyst could drastically improve its performance. These results also clearly indicate that **Mo_{60}/C**, **Mo_{28}/C**, and **Mo_{12}/C** exhibit properties that are intermediate (~100 kJ mol^{-1}) to those of Mo carbides and oxide. Notably, the EXAFS spectrum of the **Mo_{60}-aggregated/C** obtained after CHR at 773 K for 30 min (particle diameter: 1.9 ± 0.7 nm) indicated Mo carbide character, with an Mo–Mo bond length of 2.96 ± 0.02 Å (Figures S6 and S7 and Table S1) and an activation energy of ~60 kJ mol^{-1} for the RWGS (Table S2), denying the concern that the use of the TPM-DPAG4 would result in the formation of Mo oxycarbide.

Critical particle-size for Mo carbide

Figure 5a shows the particle-size dependence of the Mo–Mo bond distance. The bond length of 2.98 Å in Mo carbide was demonstrated at a particle size of above 1.4 nm, however the Mo–Mo bond is drastically shortened to 2.85–2.86 Å at that of below 1.2 nm. Thus, 1.3 nm is the critical size threshold for Mo

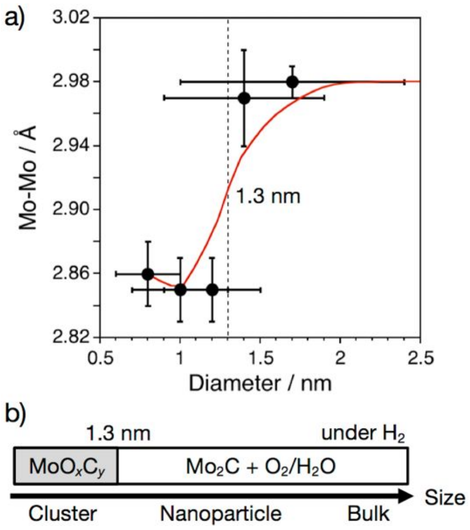

Figure 5. a) Plots for the Mo–Mo bond distance for **Mo-NP(a)/C**, **Mo-NP(b)/C**, **Mo_{60}/C**, **Mo_{28}/C**, and **Mo_{12}/C** after CHR at 773 K for 30 min, together with a smoothed trendline (red line). b) Phase diagram for the formation of Mo carbide and oxycarbide under H_2 as a function of size.

carbide particle stability; smaller particles are easily transformed into oxycarbides. Mo carbide nanoparticles with diameters of ~2 nm have been reported in many studies,[27-40] and were also observed in the present study such as **Mo-NP(a)/C**. Suslic *et al.* reported Mo carbide nanoparticles with a crystal size of 1.6 nm based on Scherrer's equation;[36] however, Mo carbide nanoparticles smaller than 1.3 nm have not been reported.

The difficulties associated with characterizing Mo oxycarbide/carbide clusters have been pointed out by several groups.[58-65] Gascon *et al*. reported that mono- or di-nuclear Mo clusters trapped in the pores of a zeolite consist of Mo oxycarbide, although those aggregated on the zeolite surface are carbide nanoparticles.[60] On the other hand, Beale *et al*. reported that Mo carbide clusters are generated in the pores of a zeolite, migrate to the surface, and aggregate to form carbide nanoparticles.[61,62] Podkolzin *et al.* proposed di- or tetra-nuclear Mo carbide clusters in a DFT calculation study on Mo clusters in a zeolite, even though the clusters were clearly bound to the O atoms of the zeolite,[63,64] suggesting their stabilization by Mo–O bond formation. These studies indicate the instability of bare Mo carbide clusters compared to aggregated carbide nanoparticles or clusters with Mo–O bonds, such as oxycarbide clusters. The critical particle size of Mo carbide stability has not yet been reported in the literature; the results of the present study show for the first time that the threshold for Mo carbide stability is 1.3 nm. It should be noted here that Wakihara and Romań-Leshkov *et al.* have reported Mo carbide clusters with a diameter of ~1 nm based on d-PDF studies.[65] However, we note that the presented d-PDF figures clearly show a shift of the Mo–Mo bonds in the clusters to shorter bond lengths compared to that of Mo carbide, which may be indicative of an oxycarbide character.

On the other hand, single-crystal x-ray structures of several Mo clusters that contain bare C atoms, such as $[MoC\{N(C(CD_3)_2Me_3)(3,5\text{-}Me_2C_6H_3)\}_3]^-$, $[Mo_3Co_3C(CO)_{18}]^{2-}$, and $[MoFe_5C(CO)_{17}]^{2-}$ have been reported by Cummins *et al.*,[66] Kamiguchi *et al.*,[67] and Muetterties *et al.*,[68] respectively. However, all these reports involve extra coordinating ligands such as NR_3 or CO, demonstrating that Mo carbide clusters readily accept extra ligands for stabilization, which in turn suggests that bare Mo carbide clusters are unstable. The exceptions are the $Mo_xC_y^+$ or MoC clusters produced via the laser ablation method under vacuum and detected in the gas phase by White *et al.*[41] and Brugh *et al.*;[42] however, such clusters have not been confirmed in the condensed phase or on supports.

In this study, the Mo oxycarbide clusters should be stabilized through bonding with both C and O atoms. Although the CHR was carried out under a high-purity H_2 flow atmosphere, an insignificant amount of O_2 (~0.02 ppm) would be sufficient for the formation of the Mo oxycarbide clusters. Above the critical particle size of 1.3 nm, Mo carbide can exist because of the presence of a sufficient number of atoms sufficient for the construction of a stable lattice or amorphous structure. Although the surface of Mo carbide might be transiently oxidized by trace O_2 contamination during CHR, the O atoms absorbed on the Mo carbide could be easily eliminated by H_2. As XPS is very sensitive to the surface chemical state of analytes, surface oxidation after CHR can be ruled out for all samples (Figure 3). Below the critical particle size of 1.3 nm, Mo oxycarbide was produced during CHR rather than by the surface oxidation of carbide. Based on our results, the size-dependence of the formation of stable Mo carbide and oxycarbide phases under H_2 is summarized in Figure 5b. Ordinary phase diagrams are based on phase behavior at the macro-scale; however, new diagrams can be obtained based on the concept of the size dependence.

Atomic movement of Mo

Figures 6a and 6b show the continuous time-course high-resolution HAADF-STEM images over 11 seconds for a Mo oxycarbide cluster (diameter = ~1 nm) and a Mo carbide nanoparticle (diameter = ~2 nm), respectively. Interestingly, the Mo atoms move within the cluster under electron-beam irradiation; similar atomic movement was also observed on the fringes of the nanoparticle. The same physical phenomenon has been reported in Au clusters and nanoparticles under electron-beam irradiation by Iijima,[19] Smith *et al.*,[20] and Batson *et al.*[21] These atomic movements could be caused by the momentum continuously provided by collisions with the accelerated electrons, particularly during observation at higher magnifications.[69] To clarify the movement of the Mo atoms and the deformation of the particles, the contours of the Mo oxycarbide cluster and the Mo carbide nanoparticle were graphed using the polar coordinate at each second as shown in Figures 6c and S8, where r_{outer} represents the sum of the atomic radii of Mo (R = 0.19 nm)[70] and r, which is the distance between the center of gravity of the particle and the center of each Mo atom. The perimeter of the particle was estimated from $\Delta\theta$ using the trigonometric function in Equation S2. Moreover, the deformation index $\Delta r_{\mathrm{outer}}(t)$ was defined as shown as Equation 1; this index represents the average change in the contour of a particle for every second.

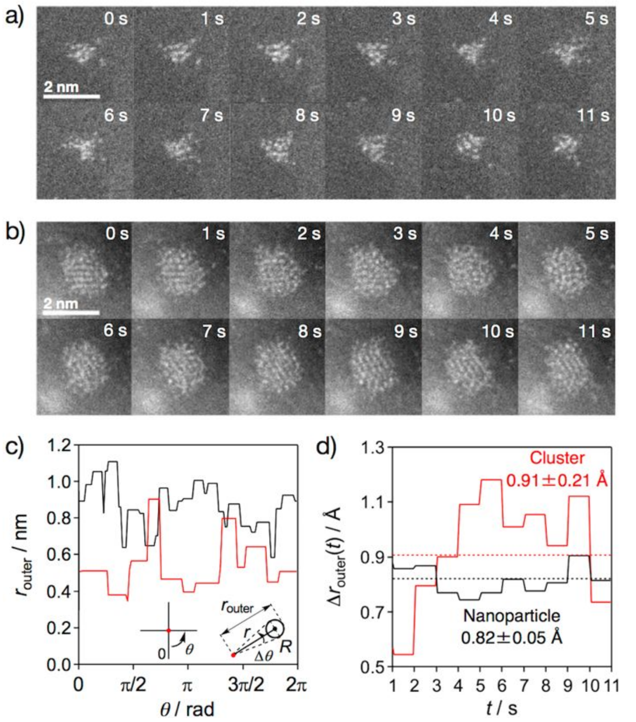

Figure 6. Continuous time-course high-resolution HAADF-STEM images obtained over 11 seconds using an accelerating voltage of 200 kV for a) a Mo oxycarbide cluster and b) a Mo carbide nanoparticle after CHR at 773 K for 30 min. c) Contour graphs of the polar coordinate with a resolution of 0.05 rad (126 points total) at t = 0 s, and d) a plot of the deformation index $\Delta r_{\mathrm{outer}}(t)$ over the 11 second period for the Mo oxycarbide cluster (red lines) and the Mo carbide nanoparticle (black lines). The inserts in c) show the polar coordinate and the outer distance (r_{outer}) centered at the center of gravity (red circles) of the cluster or nanoparticle.

In Equation 1, $\Delta r_{\mathrm{outer}}(\theta)_t$ and N_θ represent the function obtained from the contour graph at time t and the number of points for θ (126 points). Figure 6d shows the time course of $\Delta r_{\mathrm{outer}}(t)$ for the Mo carbide nanoparticle and the Mo oxycarbide cluster over 11 s. The average values of their deformation indices were estimated to be 0.82 and 0.91 Å, respectively, suggesting that the two particles exhibit almost the same average atomic displacement per unit of time. However, the standard deviations of these values, 0.05 and 0.21 Å, differ substantially, indicating a difference in the atomic movement over short periods of time. The Mo atoms on the fringes of the nanoparticle move continuously in a wobbly fashion, whereas those of the cluster move intermittently in a sudden fashion. These results suggest that the number of atoms and/or composition of the particles are responsible for the differences in atomic movement. In other words, we have quantified for the first time the atomic movement of Mo in ultrasmall nanoparticles and clusters.

Conclusions

We systematically produced Mo nanoparticles and clusters with controlled diameters of less than 2 nm on a carbon support using carbothermal hydrogen reduction at moderate temperature. Mo clusters with a size of 0.8 ± 0.2 nm were produced in a controlled fashion using the dendrimer template, which represent the smallest Mo particles with metal-to-metal bonds between Mo thus far reported. We discovered that Mo particles with diameters of 1.3 nm or greater form carbides such as β'-Mo_2C, whereas smaller particles form Mo oxycarbide. This experimental observation can be rationalized in terms of a change in the phase stability between Mo carbide and oxycarbide at a threshold value of 1.3 nm. Thus, this work demonstrated a new concept, subnano-transformation, which would be a new class of phase transformation based on the concept of the size dependence in such an ultrasmall scale. In addition, the atomic movement of Mo in a cluster and on the fringes of a nanoparticle was demonstrated under electron-beam irradiation.

Conflicts of interest

There are no conflicts to declare.

Acknowledgements

The authors acknowledge Dr. Ken Albrecht (Kyushu Univ.) for his support with the synthesis of the TPM-DPAG4, Dr. Ken Motokura (Tokyo Tech.) for his support with the XAFS measurements, and Suzukakedai Materials Analysis Division (Tokyo Tech.) for PXRD measurement. This study was performed under the approval of the Photon Factory Program Advisory Committee (proposal No. 2018G042), of the Japan Synchrotron Radiation Research Institute (proposal No. 2018B1550), and of the Kyushu Synchrotron Light Research Center (proposal Nos. 1904027F and 1910084F). This study was supported by JST ERATO Grant Number JPMJER1503 and JSPS KAKENHI Grant Numbers JP15H05757 and JP18K14237, Japan.

Notes and references

1 Ph. Buffat and J.-P. Borel, *Phys. Rev. A* 1976, **13**, 2287.
2 M. Haruta, T. Kobayashi, H. Sano and N. Yamada, *Chem. Lett.* 1987, 405.
3 G. Schmid , *Chem. Rev*. 1992, **92**, 1709.
4 M. Brust, M. Walker, D. Bethell, D. J. Schiffrin and R. Whyman, *J. Chem. Soc. Chem. Commun.* 1994, 801.
5 R. P. Andres, T. Bein, M. Dorogi, S. Feng, J. I. Henderson, C. P. Kubiak, W. Mahoney, R. G. Osifchin and R. Reifenberger, *Science* 1996, **272**, 1323.
6 M. Valden, X. Lai and D. W. Goodman, *Science* 1998, **281**, 1647.
7 S. Link and M. A. El-Sayed, *J. Phys. Chem. B* 1999, **103**, 4212.
8 Y. Sun and Y. Xia, *Science* 2002, **298**, 2176.
9 M. Kanehara, E. Kodzuka and T. Teranishi, *J. Am. Chem. Soc.* 2006, **128**, 13084.
10 A. A. Herzing, C. J. Kiely, A. F. Carley, P. Landon and G. J. Hutchings, *Science* 2008, **321**, 1331.
11 M. Turner, V. B. Golovko, O. P. H. Vaughan, P. Abdulkin, A. Berenguer-Murcia, M. S. Tikhov, B. F. G. Johnson and R. M. Lambert, *Nature* 2008, **454**, 981.
12 B. L. V. Prasad, C. M. Sorensen and K. J. Klabunde, *Chem. Soc. Rev.* 2008, **37**, 1871.
13 S. Yamazoe, K. Koyasu and T. Tsukuda, *Acc. Chem. Res.* 2014, **47**, 816.
14 A. Taketoshi and M. Haruta, *Chem. Lett*. 2014, **43**, 380.
15 S. Yamazoe, T. Yoskamtorn, S. Takano, S. Yadnum, J. Limtrakul and T. Tsukuda, *Chem. Rec*. 2016, **16**, 2338.
16 D. Eguchi, M. Sakamoto and T. Teranishi, *Chem. Sci.* 2018, **9**, 261.
17 K. Kusada, M. Yamauchi, H. Kobayashi, H. Kitagawa and Y. Kubota, *J. Am. Chem. Soc*. 2010, **132**, 15896.
18 A. Yang, O. Sakata, K. Kusada, T. Yayama, H. Yoshikawa, T. Ishimoto, M. Koyama, H. Kobayashi and H. Kitagaw, *Appl. Phys. Lett*. 2014, **105**, 153109.
19 S. Iijima, *J. Electron. Microsc.* 1985, **34**, 249.
20 D. J. Smith, A. K. Petford-Long, L. R. Wallenberg and J.-O. Bovin, *Science* 1986, **233**, 872.
21 P. E. Batson, N. Dellby and O. L. Krivanek, *Nature* 2002, **418**, 617.
22 T. Ya. Velikanova, V. Z. Kublii and B. V. Khaenko, *Sov. Powder Metall. Met. Ceram*. 1988, **27**, 891.
23 C. Giordano and M. Antonietti, *Nano Today* 2011, **6**, 366.
24 C. Giordano and T. Corbiere, *Colloid. Polym. Sci.* 2013, **291**, 1297.
25 J. R. dos Santos Politi, F. Viñes, J. A. Rodriguez and F. Illas, *Phys. Chem. Chem. Phys*. 2013, **15**, 12617.
26 M. Khazaei, M. Arai, T. Sasaki, M. Estilic and Y. Sakka, *Phys. Chem. Chem. Phys.* 2014, **16**, 7841.
27 P. Matteazzi and G. Le Caër, *J. Am. Ceram. Soc.* 1991, **74**, 1382.
28 D. Mordenti, D. Brodzki and G. Djéga-Mariadassou, *J. Solid State Chem.* 1998, **141**, 114.
29 C. Liang, P. Ying and C. Li, *Chem. Mater*. 2002, **14**, 3148.
30 R. Guil-López, E. Nieto, J. A. Botas and J. L. G. Fierro, *J. Solid State Chem.* 2012, **190**, 285.
31 B. Frank, K. Friedel, F. Girgsdies, X. Huang, R. Schlögl and A. Trunschke, *ChemCatChem* 2013, **5**, 2296.
32 L. He, Y. Qin, H. Lou and P. Chen, *RSC Adv.* 2015, **5**, 43141.
33 H. Wang, S. Liu, B. Liu, V. Montes, J. M. Hill and K. J. Smith, *J. Solid State Chem.* 2018, **258**, 818.
34 F. Wang, J. Jiang, K. Wang, Q. Zhai, F. Long, P. Liu, J. Feng, H. Xia, J. Ye, J. Li and J. Xu, *Appl. Catal. B* 2019, **242**, 150.
35 C. Wan, Y. N. Regmi and B. M. Leonard, *Angew. Chem. Int. Ed.* 2014, **53**, 6407.
36 T. Hyeon, M. Fang and K. S. Suslick, *J. Am. Chem. Soc.* 1996, **118**, 5492.
37 E. V. Matus, I. Z. Ismagilov, O. B. Sukhova, V. I. Zaikovskii, L. T. Tsikoza and Z. R. Ismagilov, *Ind. Eng. Chem. Res*. 2007, **46**, 4063.
38 D. Zeng and M. J. Hampden-Smith, *Chem. Mater*. 1992, **4**, 968.
39 J. A. Nelson and M. J. Wagner, *Chem. Mater*. 2002, **14**, 1639.
40 P. A. Alaba, A. Abbas, J. Huang and W. M. A. W. Daud, *Renew. Sustain. Energy Rev*. 2018, **91**, 287.
41 J. M. Lightstone, H. A. Mann, M. Wu, P. M. Johnson and M. G. White, *J. Phys. Chem. B* 2003, **107**, 10359.
42 D. J. Brugh, T. J. Ronningen and M. D. Morse, *J. Chem. Phys*. 1998, **109**, 7851.
43 K. Yamamoto, M. Higuchi, S. Shiki, M. Tsuruta and H. Chiba, *Nature* 2002, **415**, 509.
44 K. Yamamoto, T. Imaoka, W.-J. Chun, O. Enoki, H. Katoh, M. Takenaga and A. Sonoi, *Nat. Chem.* 2009, **1**, 397.
45 K. Yamamoto and T. Imaoka, *Acc. Chem. Res.* 2014, **47**, 1127.
46 T. Tsukamoto, T. Kambe, A. Nakao, T. Imaoka and K. Yamamoto, *Nat. commun*. 2018, **9**, 3873.
47 M. Wakizaka, T. Imaoka and K. Yamamoto, *Dalton Trans.* 2019, **48**, 14261.
48 E. Redel, R. Thomannb and C. Janiak, *Chem. Commun*. 2008, 1789.
49 C. Schöttle, P. Bockstaller, R. Popescu, D. Gerthsen and C. Feldmann, *Angew. Chem. Int. Ed*. 2015, **54**, 9866.
50 H. S. Shin, H. C. Choi, Y. Jung, S. B. Kim, H. J. Song and H. J. Shin, *Chem. Phys. Lett*. 2004, **383**, 418.
51 L. Ramqvist, K. Hamrin, G. Johansson, A. Fahlman and C. Nordling, *J. Phys. Chem. Solids* 1969, **30**, 1835.
52 C. E. Barnes, M. Ralle and S. A. Vierkötter, *J. Am. Chem. Soc.* 1995, **117**, 5861.
53 E. Clementi and D. L. Raimondi, *J. Chem. Phys*. 1963, **38**, 2686.
54 A. A. Bolzan, B. J. Kennedy and C. J. Howard, *Aust. J. Chem.* 1995, **48**, 1473.
55 Y. Xu, M. Yamazaki and P. Villars, *Jpn. J. Appl. Phys*. 2011, **50**, 11RH02.
56 I. F. Ferguson, J. B. Ainscough, D. Morse and A. W. Miller, *Nature* 1964, **202**, 1327.
57 S. T. Oyama, P. Delporte, C. Pham-Huu and M. J. Ledoux, *Chem. Lett.* 1997, **26**, 949.
58 T. Shido, K. Asakura, Y. Noguchi and Y. Iwasawa, *Appl. Catal. A Gen.* 2000, **194-195**, 365.
59 A. S. Rocha, V. T. da Silva, J. G. Eon, S. M. C. de Menezes, A. C. Faro Jr. and A. B. Rocha, *J. Phys. Chem. B* 2006, **110**, 15803.
60 I. Vollmer, N. Kosinov, Á. Szécsényi, G. Li, I. Yarulina, E. Abou-Hamad, A. Gurinov, S. Ould-Chikh, A. Aguilar-Tapia, J.-L. Hazemann, E. Pidko, E. Hensen, F. Kapteijn and J. Gascon, *J. Catal.* 2019, **370**, 321.
61 I. Lezcano-Gonzµlez, R. Oord, M. Rovezzi, P. Glatzel, S. W. Botchway, B. M. Weckhuysen and A. M. Beale, *Angew. Chem. Int. Ed.* 2016, **55**, 5215.
62 M. Agote-Arán, A. B. Kroner, H. U. Islam, W. A. Sławiński, D. S. Wragg, I. Lezcano-González and A. M. Beale, *ChemCatChem* 2019, **11**, 473.
63 J. Gao, Y. Zheng, G. B. Fitzgerald, J. de Joannis, Y. Tang, I. E. Wachs and S. G. Podkolzin, *J. Phys. Chem. C* 2014, **118**, 4670.
64 J. Gao, Y. Zheng, J.-M. Jehng, Y. Tang, I. E. Wachs and S. G. Podkolzin, *Science* 2015, **348**, 686.
65 T. Iida, M. Shetty, K. Murugappan, Z. Wang, K. Ohara, T. Wakihara and Y. Román-Leshkov, *ACS Catal*. 2017, **7**, 8147.
66 J. C. Peters, A. L. Odom and C. C. Cummins, *Chem. Comm.* 1997, 1995.
67 S. Kamiguchi and T. Chihara, *J. Clust. Sci.* 2000, **11**, 483.
68 M. Tachikawa, A. C. Sievert, E. L. Muetterties, M. R.

Thompson, C. S. Day and V. W. Day, *J. Am. Chem. Soc.* 1980, **102**, 1725.

69 T. Imaoka, T. Toyonaga, M. Morita, N. Haruta and K. Yamamoto, *Chem. Commun.* 2019, **55**, 4753.

70 E. Clementi, D. L. Raimondi and W. P. Reinhardt, *J. Chem. Phys*. 1967, **47**, 1300.

Table of Contents Entry

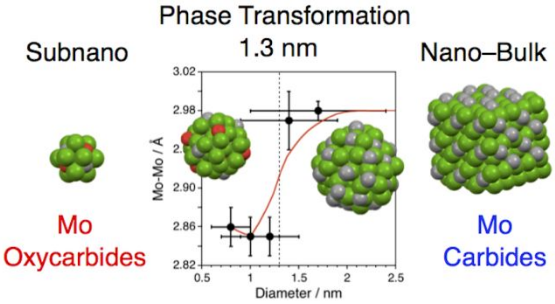

This work represents a new concept of the size dependence for phase transformation around sub-nanoscale.